Comparisons of computer simulations and experimental data for capacitive hyperthermia using different split-phantoms

Rami Muratoglu [A,B,C], Dominik Gerster [A,B,C], Jacek Nadobny [A,B,C], Alexander Hansch [A,B,C], Paul Krahl [A,B,C], Paraskevi Danai Veltsista [A,B,C], Marcus Becka[B,C], Daniel Zips [A,B,C] and Pirus Ghadjar [A,B,C]

[a] Department of Radiation Oncology, Charité – Universitätsmedizin Berlin, Berlin, Germany;
[b] Freie Universität Berlin, Humboldt-Universität zu Berlin, Berlin, Germany;
[c] Berlin Institute of Health, Berlin, Germany

Citation

Muratoglu, R. et al (2024) Comparisons of computer simulations and experimental data for capacitive hyperthermia using different split-phantoms

Oncothermia Journal 39, September 2026., 28-51.
https://oncotherm.com/MuratogluR_2024_Comparison_of_computer_simulations

Abstract

Introduction: Several positive clinical trials have demonstrated that capacitive hyperthermia (CHT) improves the effectiveness of radiation therapy for the treatment of various cancer entities. However, the ability of CHT to induce significant heating throughout the body is under debate. Objectives: To perform a pilot study involving comparisons of computer simulations and experimental data using different split-phantoms to validate hyperthermia treatment modeling for pre-planning for a clinical CHT system and to investigate the feasibility of split-phantom measurements in capacitive hyperthermia.

Materials and methods: The CHT system EHY-2030 (Oncotherm, Budapest, Hungary) was used. The system provides two electrode sizes, but only the smaller electrode, indicated as D200 electrode, was investigated in this pilot study. Horizontally and vertically splittable, different multi-slice phantoms with dielectric material properties simulating muscle and electrically low conductive fat were produced and heated. During the heating procedure, temperature-time curves were measured, and thermal images were captured. Specific absorption rate values were derived from the temperature rise (TR) values. Concomitantly, computer field simulations utilizing a detailed CAD-based model of the CHT system were performed using the simulation platform Sim4Life and compared with measurements.

Results: For the investigated electrode D200 the system power of 75W was applied, which is half of the maximum power of 150W and lies in the range of usual values for this electrode applied in patient treatments in our clinic. For 75W, a heating of 3.6°C in 6min in a depth of 1cm in an agar-based, muscle tissue-equivalent phantom was achieved. The addition of a 1cm thick, synthetic, low dielectric fat layer reduced the TR up until a depth of 8.5cm by on average around 38% (from 8.5cm onwards the absolute local TR is similar, deviations are ≤0.1°C). In terms of point-to-point absolute SAR comparison (without any normalization), up to a depth of 11cm in the phantoms central vertical plot, the simulation differs from the measured TR points by on average 25% (ranging from 7% to 36%) for the homogeneous phantom and by on average 43% (ranging from 26% to 60%) for the inhomogeneous phantom.

Conclusion: Computer simulations and experimental data were compared for the CHT system EHY-2030 using the D200 electrode, applying a thermal imaging technique for different vertically splittable phantoms. This pilot study data can be used as a guidance regarding the expected heating for this commonly used electrode size but also to further elucidate the significance of non-thermal anticancer effects. Further studies are needed for different sizes and geometries of electrodes and phantoms.

1. Introduction

Hyperthermia based on radiofrequency (RF) electromagnetic fields (EMF) is widely used in cancer treatment. For instance, hyperthermia using radiative multiple antenna or waveguidebased devices was shown to increase the effects of chemotherapy and radiation therapy in randomized controlled trials [1–4]. The anticancer effects caused by the achieved temperature increase are pleiotropic including increased oxygenation and perfusion, inhibition of DNA repair and immune effects among others [5–7]. A different approach to couple EMF to the patient body is the use of

electrodes. When electrodes are used at relatively low frequencies, i.e., below ~30MHz, the EMF energy is mainly capacitively coupled to the tissue. This technique is, therefore, known as capacitive hyperthermia (CHT) and the electrodes together with the tissue between the electrodes are part of the electric circuit. An essential characteristic of capacitive coupling is that the direction of the E-field is predominantly perpendicular to the contact surface between the electrode and the skin, as well as the subcutaneous layers. This leads to a high specific absorption rate (SAR) inside and a high-power loss at these layers, as the EMF jumps there due to the interface conditions (continuity of the normal electric flux density). This, together with the limited steering abilities when compared to radiative devices, is the reason why, subcutaneous fat poses a hindrance for capacitive devices, when intending to treat deep seated tumors [5,8].

The adjustable variables for CHT are: the choice of the electrode's size, the positioning of the electrode (including the electrode's water bolus) with respect to the treatment region and the geometry of the patient's surface, the insertion of additional water bags between the water bolus and patient's skin for better electromagnetic coupling and additional surface cooling and a proper surface cooling (also preferably including a coolant circulation for the cooling of the electrode's metallic structures) to prevent too high temperatures in the water bolus and on the skin surface and thus to enable the application of a sufficiently high energy dose [5,8]. Lastly, a separate variable is the (optional) use of amplitude modulation, as further described later on.

Several positive, randomized controlled trials demonstrated that CHT improves the effectiveness of radiation therapy for the treatment of various cancer entities [9–17]. Still, there are also studies showing no benefit from the addition of hyperthermia to radiotherapy [18]. Notably, apart from Minnaar et al. most of those trials were performed in Asian countries, where the patients generally are of a slimmer habitus. It is therefore unclear whether similar results can be achieved in western countries, where the population shows a differing body composition, since fat layers are proven to limit deep heating [8,19–21]. After all a higher thermal dose of CEM43T90>7min (CEM43T90 is CEM43 calculated for T90, T90 being the temperature, which is exceeded in 90% of the tumor; CEM: cumulative equivalent minutes at 43°C) was already shown to be a significant predictor of biochemical disease-free survival [22].

While CHT is accepted as a state-of-the-art method for superficial hyperthermia [23], its acceptance regarding its excellence in inducing significant heating throughout the body toward deeper tumor localizations is still under debate. Recently, efforts were started to develop simulation programs for several CHT systems [24] but not including the system presented in this paper. In general, comprehensive phantom studies that include measurements are rather sparse for CHT. For instance, the present authors were involved in the extended phantom measurement study for the Celsius 42 system that was used by our Berlin hyperthermia group [18]. For the system presented in this work no such study has been performed so far. One of the CHT systems is the hyperthermia device EHY-2030 (Oncotherm, Budapest, Hungary), which is clinically used in our department. In this paper, in order to compare computer simulations and experimental data using this system, we present a pilot study involving a quantitative comparison of split-phantom measurements and computer simulations for a detailed CAD-based model of the device. Concerning the fact that both, simulations and measurements, were compared in such a detailed and quantitative way, this is our knowledge the first such a study worldwide for a clinical CHT system so far. This pilot study data can be used to validate hyperthermia treatment modeling for pre-planning for a clinical CHT system and to investigate the feasibility of split-phantom

measurements in capacitive hyperthermia. Furthermore, this study may be used as a guidance regarding the expected heating for this commonly used electrode size but also to further elucidate the significance of non-thermal anticancer effects. Another goal of our work was the implementation of a framework for future treatment planning for CHT. For this, further similar studies are planned for different sizes and geometries of electrodes and phantoms.

2. Materials and Methods

2.1. Hyperthermia device

The aforementioned hyperthermia device EHY-2030 consists of the (electrically grounded) therapy bed, on which the patient lies and the upper "active" electrode, which is connected to the amplifier channel and can be placed onto the patient's treatment region by moving the electrode's rotatable arm. The operating frequency of the system is 13.56MHz.

The upper electrode can be detached from its arm and exchanged for a different-sized electrode. The commercial system provides two electrode sizes but only the smaller electrode, indicated as 'D200 electrode', was investigated in this pilot study. The D200 electrode has a diameter of around 20cm and the system allows to drive this electrode with a maximum forward power of 150W. The system may also be connected to a bigger electrode of around 34cm diameter (indicated as 'D300 electrode'), that is driven by a maximum forward power of 250W. Further investigations involving the bigger electrode are planned in the next future, however this requires bigger phantoms, which were not available for this pilot study.

2.2. Phantom rationale and design

Different multi-slice phantoms were produced similar to those recommended by the European Society for Hyperthermic Oncology (ESHO) guidelines for superficial hyperthermia [23]. At this point, it is worth noting that the main aim of this study was not to judge the thermal effectivity of this system via strictly fulfilling the procedures and temperature limits defined by the ESHO guidelines. This study has to be understood as a pilot study to check the feasibility of the phantom production and use of the splitting technique, as well as to perform comparisons with numerical results (see Section 4). However, with respect to the geometry requirements, we designed our experiments based on the information provided by the ESHO guidelines. According to the guidelines, the phantom should be twice the size of the used applicator electrode in the lateral dimensions and the thickness of the phantom should be at least three times the expected penetration depth. With a cylindrical phantom of a diameter of 45cm and a thickness of 22cm, we fulfilled both phantom size requirements for the D200 electrode. The large D300 electrode would require larger phantoms in lateral directions and thus the construction of bigger casting molds, so we decided to focus on the D200 electrode in this pilot study.

The thickness of 22cm was made up of a 20cm thick agar cylinder in the center with two additional 1cm thick layers, which enclose the phantom on the top and at the bottom. For comparison, two cases for these 1cm thick layers were investigated: one with an in-house produced synthetic fat layer and another with a layer made up of agar gel. To the phantom with the synthetic fat layer, we here refer to as the 'inhomogeneous' phantom (details see Section 2.4) and the phantom with the

agar-based layer is in the following referred to as the 'homogeneous' phantom (details see Section 2.3). With the phantoms' increased total thickness and the additional 1cm thick layers, made up of a synthetic fat layer in the inhomogeneous phantom, not only at the top but also at the bottom of the phantoms, we also aimed to mimic a real patient's condition.

Furthermore, similar to the phantom construction recommended in the ESHO guidelines our multi-slice phantoms were splittable in their vertical plane and the horizontal layers could also be removed, thus allowing temperature measurements using a thermal camera through the central vertical and a horizontal plane between the 1cm thick layer and the rest of the phantom.

With good accuracy, the phantom's density was assumed to be ρ = 1000kg/m3 [21,25]. It had a weight of around 35kg.

For the fabrication of our phantoms, using a 3D print technique, we constructed a special casting mold, in which the heated agar gel was filled and left to cool down (Figure 1). The casting mold was 3D-printed part by part using polycarbonate. The single parts were then screwed together with stainless steel screws. The casting mold was designed to produce one half of the cylindrical, muscle tissue-equivalent phantom allowing us to then put two halves together to receive a complete phantom and, after the heating experiment, to easily split it vertically in two halves for the thermal imaging. The phantoms were assembled without any additional, disturbing layer or material in between.

The additional 1cm thick layers were cast in two cooking pans (diameter of 45cm). This was done to parallelize the casting of the different phantom parts and was especially important for the synthetic fat layers, since the reached temperatures in their production would have been too high for the polycarbonate casting mold to withstand.

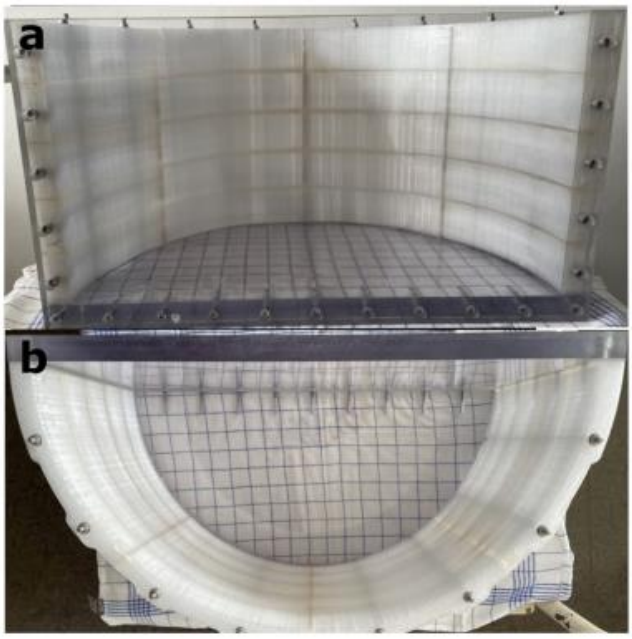

Figure 1. (a) View from the planar side onto the casting mold and (b) view from above onto the casting mold.

2.3. Multi-slice, homogenous phantom

For the creation of the 20cm thick muscle tissue-equivalent phantom, that forms the basis of both the homogeneous and inhomogeneous phantom, the recipe [25] recommended in the ESHO guidelines for superficial hyperthermia [23] was followed (Table 1).

First the sodium chloride was dissolved in the deionized (DI) water. The solution was heated until 50–60°C. Next, the agar was slowly added while stirring the mixture and heating it at 80–90°C for around 5min. After that, the mixture was slowly filled into the casting mold up to the 20cm thickness mark. It was then left to cool down, solidify and was ready to be used in approximately 24h. This procedure was repeated for the second half of the agar cylinder. For the homogeneous phantom a third repetition of the cooking process was done for the remaining two 1cm thick agar layers, where the heated agar gel was evenly filled into two cooking pans up to the 1cm mark. Finally, the two agar layers were positioned below and on top of the 20cm thick muscle tissue-equivalent phantom to form the complete multi-slice, homogeneous phantom with a thickness of 22cm.

2.4. Multi-slice, inhomogeneous phantom

For the multi-slice, inhomogeneous phantom, a recipe from a recent publication [26] was applied (Table 2) [26].

It must be emphasized that continuous stirring of the mixture was necessary during all the following steps. First, the oil and the glycerol were mixed at room temperature in a cooking pot placed on a powerful enough cooking plate. It was made sure that no air bubbles were present in the resulting gel. After around 10min, a uniform emulsion was obtained. As next, the emulsion's temperature was gradually increased to 130°C. Once 130°C was reached, the ethylcellulose was gradually added until it was dissolved. Next, the pot was partly covered to minimize the dispersion of vapors, and the temperature was increased to 170°C. Finally, the mixture was evenly poured into the two cooking pans up to the 1cm thickness mark and was left to cool down.

After cooling down, the two synthetic fat layers were ready to be used and placed on top and at the bottom of the 20cm thick muscle tissue-equivalent phantom to create a finished inhomogeneous phantom with a thickness of 22cm (Figure 2).

Table 1. Quantities used in the production of the muscle tissue-equivalent phantom following the publication from [25].

Substance	Quantity
Sodium chloride	3.3 g
DI water	Around 956 g
Agar powder	40 g

Table 2. Quantities used in the production of the synthetic fat layer following the publication from [26].

Substance	Quantity in wt%
Canola oil	36
Ethylcellulose	7
Glycerol	36

2.5. Heating procedure

For the temperature measurements the two halves of the muscle tissue-equivalent phantom were placed on the applicator table with the 1 cm thick additional layers, either the agar or the synthetic fat layer, at the bottom and at the top of the phantom (Figures 3 and 4). The upper electrode was then positioned centrally on the phantom. It was taken care that full contact was established between the device and the phantom. The electrodes coolant temperature was equal to the room temperature being 20 °C.

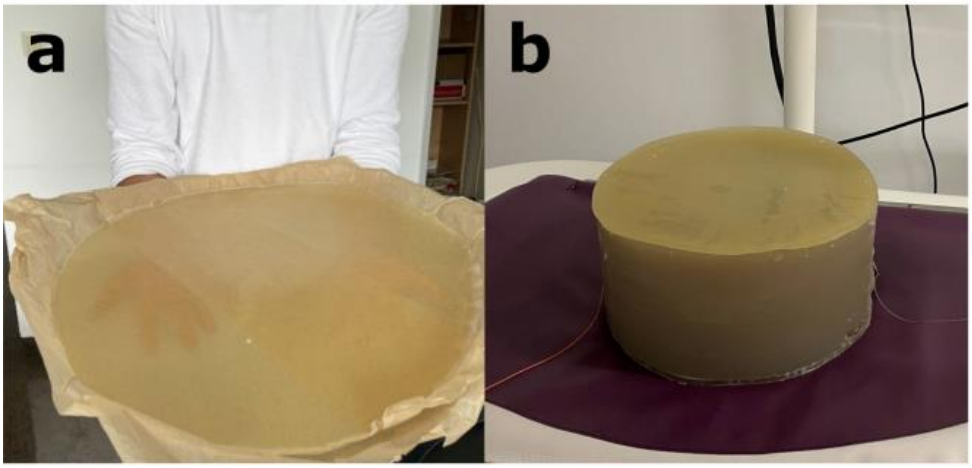

Figure 2. (a) In-house produced, synthetic fat layer with a thickness of 1cm and a diameter of 45cm and (b) assembled inhomogeneous phantom, consisting of the muscle tissue-equivalent phantom (diameter 45cm, height 20cm) in the center and two additional 1cm thick synthetic fat layers on the top and at the bottom.

Figure 3. Assembled inhomogeneous phantom during a heating procedure with the EHY-2030. The phantom has 4 parts. A circular agar cylinder (diameter 45 cm, height 20 cm) is built from

two vertically splittable, half-cylindrical parts (darker color). This cylinder is horizontally bounded by two 1 cm thick top and bottom layers of circular shape (diameter 45 cm, lighter color), consisting of either agar gel (homogeneous phantom) or synthetic fat (inhomogeneous phantom), like in this picture. The metallic structures of the upper electrode (D200) are located behind the cylindrical (white) plastic cover and are cooled by a system with a circulating coolant at a constant temperature of around 20 °C. Between the cooled metallic electrode parts and the phantom, there is a cylindrical bolus that contains DI water and is surrounded by a silicon cover (purple color) and a special conductive textile material. The water in this bolus is not part of the system's circulating coolant. For further detailed information, see, Figure 4.

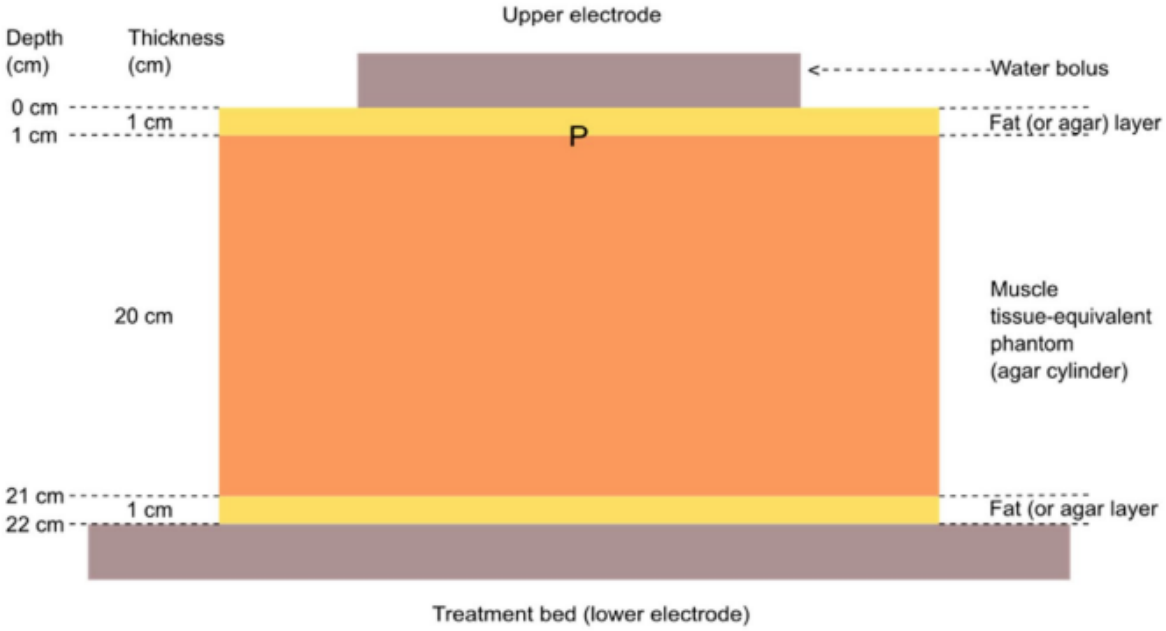

For the heating procedure we chose 6min, which is also the heating time recommended by the ESHO guidelines (note again, that the main aim of this paper was not to judge on the thermal effectivity of this system via a strict fulfillment of the procedures and temperature limits defined by the ESHO guidelines, see the discussion section). We applied 75W, which is half the D200 electrode's maximum power output of 150W (75W lies in the range of usual average values applied in clinical treatment for this electrode in our clinic). Inside the phantom the TR is with a good accuracy proportional to the applied power, thus the results for maximum power output of 150W can be, if necessary, easily obtained by multiplying the TR result by a factor of 2. Detailed information about the validity of this 'power scaling' for measurements can be found in Section 2.8, below. Prior to each measurement the phantom, and all thermally relevant system parts like the electrode's water bolus, were left to cool down again to room temperature. For further details, see also the legends of Figures 3 and 4.

2.6. Temperature measurement procedure

The utilized thermal camera was the FLIR 8E-TX (Teledyne FLIR, Frankfurt am Main, Germany) with a heat sensitivity (NETD) of <0.05°C and a temperature accuracy of ± 2%. The used thermal probe is the fiber optic temperature sensor OTG-MPK5 (opSens-Solutions, Quebec, Canada) with a temperature accuracy of ± 0.3°C and a reaction time of 225ms. The time between each registered measurement point of the thermal probe was set to the lowest possible interval of 2.8s. It was

aimed to position the probe in a depth of 1cm. This was done by pinching it in between the two halves of the muscle tissue-equivalent phantom (Figure 4) (the depth of 0cm is the top surface of the fat (or agar) layer, i.e., the contacting surface to the electrode's water bolus).

Before the heating procedure, temperature measurements were performed. Thermal images were taken of the horizontal plane in 1cm depth after removing the upper layer, and of the central vertical plane by splitting the phantom open in its two halves. The temperature probe measurements were continuously monitored 1min before the heating and during the heating.

After six minutes of heating, the upper electrode together with the upper 1cm thick layer was swiftly removed and again a thermal image of the horizontal plane was captured. Next, the phantom was quickly split open and a thermal image in the vertical plane through the phantom was captured. It was taken care and ensured that those measurements were completed within 15s.

After the phantom had fully cooled down, it was assembled again for the next heating procedure. For each of two phantoms, two experiments were performed, respectively.

The thermal images were assessed with FLIR Thermal Studio (Teledyne FLIR, Frankfurt am Main, Germany). In that software, the fit between the image and the overlaid thermal image was further adjusted and optimized.

After that the measurement points, for which the temperature was assessed in the software, were positioned on an axis through the captured horizontal or vertical plane. Finally, the TR was obtained by subtracting the given temperature in two corresponding measurement points in the thermal image before and after the treatment.

2.7. Determination of the TEFS and TEPD from the TR

The thermal effective field size (TEFS) is defined as the area within 50% of the maximum TR, observed in the horizontal plane at 1cm depth in the phantom [23].

The thermal effective penetration depth (TEPD) is defined as the depth, at which the TR drops to 50% of the maximum TR measured in 1cm depth [23].

2.8. Determination of the SAR from the TR (relationship between SAR and TR)

2.8.1. Conductive heat transfer equation

In the case of our measurements in non-perfused phantoms the relationship between TR and SAR is described with good accuracy by the conductive heat transfer equation, which can be derived from the bioheat transfer equation (BHTE), originally formulated by Pennes [27]. Thus, starting, for instance, from the BHTE notation used in Equation (1) in [28], we obtain the following conductive heat transfer equation, which with good accuracy describes temperature behavior in our phantoms during heating:

$$\rho \cdot c \cdot \frac{\partial T}{\partial t} - \nabla \bullet (\kappa \cdot \nabla T) \approx \rho \cdot \mathrm{SAR}. \qquad (1)$$

where t is the time in seconds, T is the temperature in kelvins with the known initial condition T(t=0), ρ is the density in kilograms per cubic meters, c is the heat capacity in watts times seconds per kilograms per kelvins, κ is thermal conductivity in watts per meters per kelvins, and SAR is the specific absorption rate in watts per kilograms. In general, the SAR in Equation (1) can be time-dependent, but in our experiments, it is with good accuracy a constant value during heating.

2.8.2. Power scaling

The temperature distribution T in Equation (1) can be formulated as a sum of a 'basal' temperature T0 (T before heating) and a temperature rise distribution TR. As shown in [28] in the Equations (5a) and (5b), when certain conditions are fulfilled, the relationship between TR and SAR is linear, i.e., if, for instance, twice the power is applied and consequently each SAR value is doubled in any point, as a result the TR value in these points is doubled, too. We refer to this linear relationship in this paper as 'power scaling'. We used the principle of power scaling for determining the TR values that would be obtained by utilizing the maximum power (150W) from our TR measurements done with half the system's maximum power (75W).

In the case of numerical calculations, the validity of this power scaling procedure is explained in [28] in Equations (5a) and (5b). In the case of measurements, the power scaling principle is valid for any power used, when, firstly, the material constants like the thermal conductivity and heat capacity do not change their values during heating, and secondly, the boundary conditions (BC), as well as the initial conditions are the same for any power applied (basal T0 remains the same). As to the first necessary condition: as shown in [29], for the temperatures in the range of 20–30°C, covering the temperatures reached in our experiments, the material properties can be assumed as temperature-independent. As to the second condition: This condition is of course 'automatically' fulfilled because we change only the power applied to the system, but the initial conditions (certain phantom temperature distribution before heating) are by definition the same. Furthermore, the same BC for any applied power means, that in the case of a Dirichlet-type BC the same temperature at the phantom's surface is present (for instance a room temperature of constantly 20°C), and/or that in the case of the Cauchy-type heat transfer BC, the same exterior temperature (in our case 20°C) and the same (and temperatureindependent) value of the outward heat transfer coefficient are given. Again, with good accuracy, it can be assumed that in the range between 20°C and 30°C the outward heat transfer coefficient remains constant. Moreover, the room temperature is constantly held at 20°C via the air conditioning in our clinic.

Another good illustration of the validity of power scaling is the general possibility of the use of the Green's function (GF) representation for Equation (1). The GF describes the temperature distribution caused by an instantaneous, local heat pulse [30]. Again, the power scaling is possible if the GF is dependent only on the geometry and material parameters, but not on the temperature, i.e., particular material properties like the heat capacitance and thermal conductivity must not be temperature-dependent in the thermal range of interest (20–30°C). In conclusion, power scaling can be used with good accuracy for our phantoms because of the linearity of the problem described in Equation (1) under the assumption of temperature-independent material properties.

2.8.3. Formulation without conduction term for the SAR determination from the TR ('temperature-rise method'). Restrictions for comparison between measurements and calculations

A very often applied way to create a simple and direct relationship between SAR and TR values that allows a direct determination of SAR from TR (and vice versa) is an assumption, that in some points of the investigated domain, the term $\nabla \bullet (\kappa \cdot \nabla T)$ in Equation (1) can be neglected [31]. Consequently, in these points the heat conduction Equation (1) gets reduced to a simple formula: $c \cdot \frac{\partial T}{\partial t} \approx SAR$. When SAR values do not change during heating, $\frac{\partial T}{\partial t}$ can be replaced by $TR/\Delta t$, where Δt is heating time (in our case Δt= 6 min). Subsequently, the following simple formula (often referred to as 'temperature rise method') can be obtained for the determination of the SAR from the TR:

$$SAR \approx c \frac{TR}{\Delta t} \quad (2)$$

Points, for which the approximation in Equation (2) is appropriate, may be used for determination of SAR values from measured TR values. In our case, these experimentally derived SAR values were compared to the calculated SAR values, as shown in Section 3.3. For points that are situated in our agar-based muscle tissue-equivalent phantom material, for which we applied Equation (2), we inserted the heat capacitance c=4184J/kg × C [25]. The procedure described in Equation (2) is true with good accuracy for points that are not situated near electromagnetic and/or thermal boundaries, like the phantom's surface or interfaces between different media like between the agar gel and the synthetic fat. At such interfaces, firstly, electromagnetic properties may abruptly change and thus the SAR may 'jump' or exhibit sharp 'hot spots' that may lead to steep temperature gradients and hence may generate a heat conduction. Secondly, thermal material properties may also abruptly change and therefore a measured TR value in a point near an interface may be related not only to one single medium, but to two media, situated on both sides of the interface, and this relationship may be very complex or even unclear. Consequently, we applied the formula in Equation (2) only to those points that are located in a distance of at least 1cm from thermal and/or electromagnetic boundaries/interfaces.

2.9. Simulation procedure

For the phantom measurements, corresponding simulations for the calculation of RF-EMF were performed using the simulation platform Sim4Life (ZurichMedTech, Zurich, Switzerland). Due to a relatively low operating frequency of 13.56MHz and as a result a very large wavelength in comparison to the geometry size, the influence of the magnetic field can be neglected and therefore a fast Sim4Life solver, using a quasi-static electromagnetic approximation of the Maxwell's equations, was applied.

Accurate computer-aided design (CAD) models of the applicator device and its electrode were provided by the manufacturer (Oncotherm, Budapest, Hungary) (Figure 5). Moreover, computed

tomography (CT) scans of the phantoms were acquired, from which accurate 3D models were derived. This was done by exporting the CT scans as polygons and converting them into 3D voxel models with an equal resolution to the CT data, using the software Plastimatch (The General Hospital Corporation, Massachusetts, USA) and an in-house written code in Matlab (The MathWorks, Inc., Massachusetts, USA).

Finally, the simulation results were exported and the SAR for the different depths were read out in a .xlsx file. After this, the percentual difference between the measured and simulated SAR at the different depths was determined.

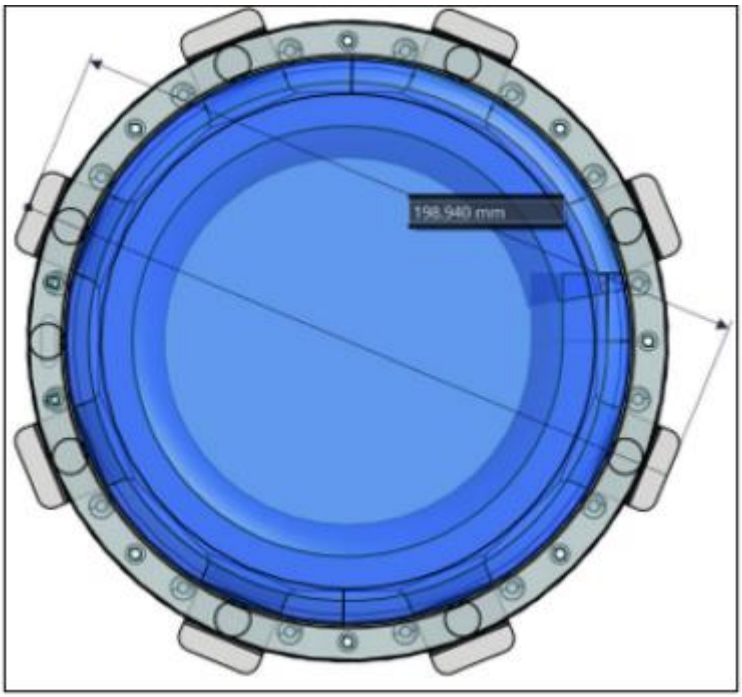

Figure 5. Computer-aided design (CAD) model of the electrode D200 of the hyperthermia system EHY-2030, containing complex conductive textile and bolus parts attached to a metal ring structure.

3. Results

3.1. Dielectric property assessment

Prior to the measurements, we needed to assess the accurate dielectric properties of the used materials in our measurements, to insert them into our simulation settings (Table 3).

For this, the DAKS-12 (SPEAG, Zurich, Switzerland) was acquired and implemented into our experimental workflow. For Table 3, there is worth noting, that with an electrical conductivity of 0.54S/m and a relative permittivity of 78.52 we were well in the range of the reported values in the literature [23, 25].

Concerning our low dielectric synthetic fat layer, the original publication introducing our followed recipe already reported lower dielectric values than the ones of real fat for our investigated

frequency range, with the electrical conductivity being 36 times lower and the relative permittivity being 1.5 times lower than the literature values for real fat tissue [26]. The measurements of our own fat layers showed even lower dielectric properties, with the electrical conductivity being smaller by a magnitude of two powers of ten and the relative permittivity being 31% lower than those reported in [26].

3.2. Temperature measurements

With an applied power of 75W for 6min, the measurements show a TR of 3.6°C in 1cm depth in the central plot of the homogeneous phantom (Figure 6). The TR for the inhomogeneous phantom at that depth in the central plot is 2.3°C. As aforementioned, however, 75W is only half of the maximum power available for this electrode. Thus, to make a statement for the device's maximum capabilities, those results must be scaled to the device's maximum power output of 150W, resulting in a TR of 7.2°C for the homogeneous and 4.6°C for the inhomogeneous phantom (for power scaling, see Section 2.8.2). For the homogeneous phantom at 75W a TR of 1.8°C was observed up to a depth of between 2.3 and 2.9cm and for 150W up to between 4.1cm to 4.8cm.

For the inhomogeneous phantom, this is the case up to a depth of between 1.6 and 2.3cm for an applied power of 75W and up to a depth of between 2.9 and 3.5cm for an applied power of 150W.

A TEPD of 2.3 to 2.9cm was measured for the heating procedure with the homogeneous and 2.9 to 3.5cm for the inhomogeneous phantom. The averaged TEFS are 178cm2 for the homogeneous phantom and 254cm2 for the inhomogeneous phantom (Figure 8a and b and Supplementary Figure 1).

Table 3. Measured dielectric properties with the DAKS-12. SD is the standard deviation.

Material	Electrical conductivity (S/m)	Relative permittivity
Muscle tissue-equivalent phantom (agar gel) (16 averaged measurements)	0.54 (SD 0.015)	78.52 (SD 3.246)
Synthetic fat layer (6 averaged measurements)	0.514×10^{-3} (SD 1.158×10^{-5})	11.34 (SD 0.224)
DI water	0.1758×10^{-3}	76.74
Silicone	0.3275×10^{-4}	3.41
Leatherette (on the applicator table)	0.12×10^{-3}	4.13

Obviously, the synthetic fat layer causes that some parts of the energy are directed in the horizontal direction instead of penetrating toward the perpendicular direction, which can be observed by comparing the TEFS for both phantoms.

Note that for the TEFS determination of the homogeneous phantom the TR values in the 1cm deep horizontal plane were used (Supplementary Figure 1). In the case of the inhomogeneous phantom a depth of 1cm would be at the interface between the upper 1cm thick fat layer and the muscle tissue-equivalent phantom. Since the TEFS and TEPD determination has to be done in reference to the max TR 1cm deep inside the muscle tissue-equivalent phantom, the measured TR values in the vertical plane at 2.3cm depth and thus at 1.3cm depth inside the muscle tissue-equivalent phantom were utilized in the case of the inhomogeneous phantom (Figure 8b).

On one hand the TR measurement recorded with our thermal probe for the inhomogeneous phantom, being 2.4°C (SD 0.43), corresponds well to the one measured with the thermal camera. The thermal probe measurement for the homogeneous phantom on the other hand, being 2.08°C (SD 0.23), corresponds well to the measured one with the thermal camera in a depth somewhat deeper than 1cm. This was due to the fact that for the placement of the thermal probe, no fixated catheter inside the phantom was utilized. This was done to prevent disruptive effects on the EMF by additional material boundaries. Instead, the thermal probe was pinched in between the two muscle tissue-equivalent phantom halves. This made an accurate positioning in 1cm depth difficult and led to the thermal probe's position being somewhat deeper than 1cm.

3.3. Comparison to the simulations

Figure 7 shows the comparison between the measurements and the simulations in terms of absolute SAR (as pointed out in Section 2.8.3, for measured data, the SAR is derived via the TR by Equation (2) using the thermal capacity of agar gel of c=4184J/kg×C). The simulations refer to the absorbed power of 75W in the total calculation domain, which was the power used for measurements as shown in Figure 6 in terms of the TR. Note that for the inhomogeneous phantom measurements, only from a depth of 2.3cm onwards up until 18.5cm the TR derived SAR values can be used for a robust comparison. As explained at the end of Section 2.8.3, we apply the formula in Equation (2) for this comparison only to those points that are located in a distance of at least 1cm from thermal and/or electromagnetic boundaries/interfaces, with the interface between fat and agar being situated at 1cm and 21cm depth. The results are presented in terms of absolute SAR (i.e., not nominalized to any maximum value like the SAR at depth 1cm, etc.). At the depths of 1cm, 1.6 and 2.3cm the simulated SAR is higher than that derived from measured TR values via Equation (2) by 7% (3W/kg), 18% (6.8W/kg) and 24% (7.4W/kg) for the homogeneous phantom. For the inhomogeneous phantom at the depth of 2.3 the simulated SAR is 26% (6W/kg) higher. The absolute SAR difference on average is only 3.7W/kg (ranging from 0.6 to 8W/kg) for the homogeneous phantom across all measurement points and 4.3W/kg (ranging from 0.6 to 8.7W/kg) for the inhomogeneous phantom from 2.3cm on up until 18.5cm depth. Up to a depth of 11cm the simulation differs from the measured TR points by on average 25% (ranging from 7% to 36%) for the homogeneous phantom and by on average 43% (ranging from 26% to 60%) for the inhomogeneous phantom. From a depth of 13.5cm on, the simulations start to differ from the measurements by more than 60%. Since the SAR in the depth is very small, even very little differences of around 1.5W/kg lead to a high relative difference. Thus, with increasing depth inside the phantom, the absolute SAR difference becomes more meaningful.

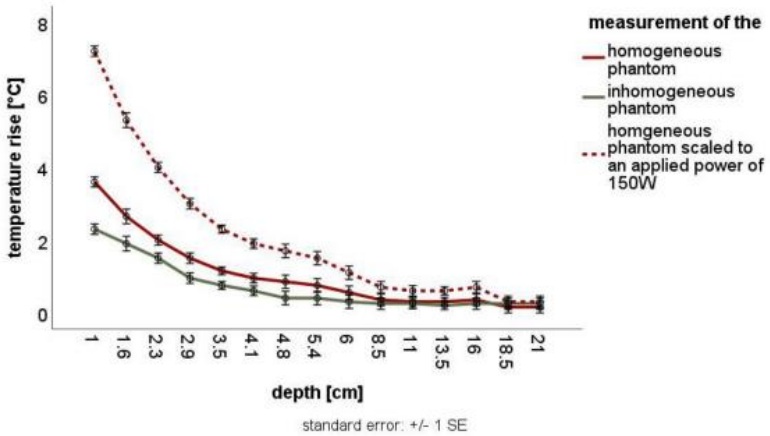

Figure 6. Measured TR for the D200 electrode driven using 75W (half of the maximum possible power output of 150W for this electrode) in the central vertical plane (along the rotational phantom's symmetry axis perpendicular to the electrode) through the phantoms in dependence of the depth from the top to the bottom of the phantoms. Two experiments were done for each phantom. (the depth of 0 cm is the top surface of the fat (or agar) layer of 1 cm thickness, i.e., the contacting surface to the electrode's water bolus. Thus, the depth of 1 cm is the interface between the top fat (or agar) layer of 1 cm thickness and the vertically splittable circular agar cylinder (diameter 45 cm, height 20 cm). The depth of 21 cm is the interface between the circular agar cylinder and the bottom fat (or agar) layer of 1 cm thickness.).

The simulation of the homogeneous phantom shows a TEPD of around 3.3cm and the simulation of the inhomogeneous phantom a TEPD of around 4.1cm, which is for every phantom type around 0.5cm higher than the TEPD determined from measurements. For the depth of 0 and 0.5cm (these points are not shown in Figure 7) and an applied power of 75W, the simulation shows a SAR of 59 and 54W/kg for the homogeneous phantom. For the inhomogeneous phantom, around 131W/kg is simulated at both, 0 and 0.5cm depth. Note, furthermore, in Figure 7, that, for the homogeneous and inhomogeneous phantom, the initial SAR decay (in the depth between 1 and 2.3cm) is steeper for the measured data than for the calculations.

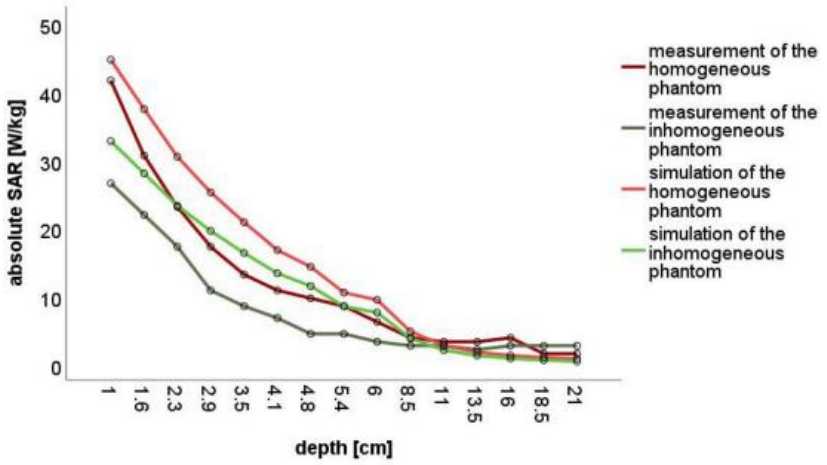

Figure 7. Absolute SAR through the central vertical plane (along the rotational phantom's symmetry axis perpendicular to the electrode) of the phantoms derived from measurements via Equation (2) and the corresponding simulations in dependence of the depth for a total power of 75W. The standard error for the measured values is given in Figure 6. For the depth of 0 and 0.5 cm (these points are not shown in Figure 7) and an applied power of 75W, the simulation shows a SAR of 59 and 54W/kg for the homogeneous phantom. For the inhomogeneous phantom, around 131W/kg is simulated at both, 0 and 0.5 cm depth. Note that for the inhomogeneous phantom measurement only the depicted SAR values from a depth of 2.3 cm onwards up until 18.5 cm are reliable as a distance of at least 1 cm to the fat/agar interface is required for Equation (2) to be applicable. (the depth of 0 cm is the top surface of fat (or agar) layer of 1 cm thickness, i.e., the contacting surface to the electrode's water bolus. Thus, the depth of 1 cm is the interface between the top fat (or agar) layer of 1 cm thickness and the vertically splittable circular agar

cylinder (diameter 45 cm, height 20 cm). The depth of 21 cm is the interface between the circular agar cylinder and the bottom fat (or agar) layer of 1 cm thickness.).

Figure 8a) TR homogeneous phantom														
depth	horizontal position [cm]													
[cm]	-19.5	-16.5	-13.5	-10.5	-7.5	-4.5	-1.5	1.5	4.5	7.5	10.5	13.5	16.5	19.5
1	0.15	0.35	0.65	1	2.9	3.85	3.75	2.95	3.2	2.6	0.65	0.45	0.3	0.2
2.3	0.05	0.1	0.25	0.65	1.25	1.95	2.05	1.5	1.25	0.9	0.35	0.1	0.05	0.05
3.5	0	0.05	0.15	0.35	0.6	0.95	1.1	1	0.75	0.45	0.1	0.1	0	0
6	0.05	0.05	0.15	0.25	0.4	0.55	0.55	0.6	0.5	0.25	0	0	0.05	0
8.5	0	0.05	0.1	0.3	0.3	0.4	0.45	0.4	0.35	0.1	0	0	0	0.2
11	0	0.05	0.1	0.25	0.2	0.35	0.3	0.35	0.25	0.15	0	0.05	0	0
13.5	0	0.05	0.2	0.3	0.2	0.25	0.35	0.3	0.2	0.2	0.05	0	0.05	0
16	0.1	0.15	0.25	0.3	0.2	0.3	0.3	0.25	0.2	0.2	0.05	0	0	0
18.5	0.2	0.25	0.15	0.2	0.15	0.15	0.15	0.2	0.15	0.15	0.1	0.15	0.1	0.05
21	0.2	0.2	0.15	0.25	0.15	0.15	0.1	0.15	0.15	0	0.05	0.1	0.05	0.3

Figure 8b) TR inhomogeneous phantom														
depth	horizontal position [cm]													
[cm]	-19.5	-16.5	-13.5	-10.5	-7.5	-4.5	-1.5	1.5	4.5	7.5	10.5	13.5	16.5	19.5
1	0.5	0.55	0.6	0.95	1.8	2.95	2.5	2.55	2.6	2	1	0.65	0.4	0.2
2.3	0.3	0.35	0.4	0.6	1.3	1.75	1.45	1.6	1.45	0.9	0.55	0.4	0.35	0.3
3.5	0.25	0.3	0.3	0.4	0.7	0.85	0.7	0.85	0.7	0.4	0.3	0.3	0.3	0.2
6	0.25	0.25	0.3	0.3	0.3	0.3	0.3	0.3	0.3	0.3	0.3	0.35	0.3	0.2
8.5	0.25	0.2	0.3	0.3	0.25	0.3	0.3	0.2	0.3	0.25	0.3	0.3	0.3	0.2
11	0.15	0.25	0.3	0.25	0.25	0.3	0.25	0.3	0.35	0.3	0.35	0.3	0.3	0.2
13.5	0.2	0.2	0.3	0.25	0.25	0.25	0.25	0.25	0.3	0.3	0.35	0.3	0.3	0.2
16	0.25	0.25	0.3	0.25	0.25	0.25	0.25	0.25	0.3	0.2	0.3	0.3	0.3	0.2
18.5	0.25	0.25	0.3	0.25	0.25	0.25	0.2	0.2	0.25	0.25	0.3	0.2	0.3	0.25
21	0.25	0.25	0.3	0.25	0.3	0.25	0.2	0.3	0.25	0.2	0.3	0.25	0.25	0.2

Figure 8. (a and b) Matrices of the measured TR for the D200 electrode driven using 75W (half of the maximum possible power output of 150W for this electrode) in the central vertical plane (along the rotational phantom's symmetry axis perpendicular to the electrode) through the homogeneous (a) and inhomogeneous (b) phantom in dependence on the depth from the top to the bottom of the phantoms. Two experiments were done for each phantom. (the depth of 0 cm is the top surface of the fat (or agar) layer of 1 cm thickness, i.e., the contacting surface to the electrode's water bolus. Thus, the depth of 1 cm is the interface between the top fat (or agar) layer of 1 cm thickness and the vertically splittable circular agar cylinder (diameter 45 cm, height 20 cm). The depth of 21 cm is the interface between the circular agar cylinder and the bottom fat (or agar) layer of 1 cm thickness. The average standard error for the two measurements done is 0.115 or the homogeneous phantom (a) and 0.27 for the inhomogeneous phantom (b).

3.4. Comparisons on central vertical planes

In Figures 8a andb and 9a–d comparisons are shown in the form of 'matrices' for the measurements and simulations for both phantoms in their central vertical planes, depicting the TR and the SAR, as further insightful information can be drawn from them.

For both, the simulations and the measurement of the two phantoms, a decrease in TR and SAR can be observed from the center of the upper electrode onwards to the bottom and to the sides of the phantom. In both the y- and the x-axis the maximum TR and SAR is achieved in a 4.5cm radius around the center of the upper electrode.

Referring to the presented matrices, similar to the results from 3.3, a better agreement between measurements and simulations is given up to a depth of 11cm.

For an evaluated radius of 7.5cm the average relative difference between simulated and measured SAR [derived from the measured TR via Equation (2)] is 25% for the homogeneous and 42% for the inhomogeneous phantom. The absolute difference is on average 3.61W/kg for the homogeneous and 3.12W/kg for the inhomogeneous phantom.

When increasing the evaluated radius to 10.5cm, the relative difference is 35% for the homogeneous and 58% for the inhomogeneous phantom. The absolute difference then is 3.18W/kg for the homogeneous and 2.79W/kg for the inhomogeneous phantom.

From a depth of 13.5cm on and with a larger evaluated radius reaching the average relative difference even exceeds 100%. Since the SAR in the depth and toward the edges of the phantom is small, this still translates to rather small absolute differences (Figure 9).

4. Discussion

The comparisons between numerical and experimental data using split-phantoms were performed for the EHY-2030 system utilizing the D200 electrode at 75W (which is half of the maximum power of 150W for this electrode and lies in the range of usual values for this electrode applied in patient treatments in our clinic) results in a TR of 3.6°C in 6min in 1cm depth in the muscle tissue-equivalent (homogeneous) phantom in its central plot in the central vertical plane. For the maximum power of 150W, when applying the power scaling procedure explained in Section 2.8.2, this is with good accuracy equivalent to a heating of 7.2°C in 6min in a depth of 1cm. The results for the homogeneous phantom in its central plot in the central vertical plane show that at the maximum power output of 150W a TR of at least 1.8° in 6min (corresponding to a SAR of around 20W/kg, which is a value comparable to moderate values used in deep hyperthermia applications, see, e.g., Table 1 in [31]) can be obtained up to a depth of around 5cm. For the inhomogeneous phantom, this is the case up to a depth of 3.5cm.

To achieve a TR of 6°C, in the central plot in the central vertical plane, a depth of 1, 2 and 3cm a power output of around 125, 194 and 319W would be needed for the D200 electrode in the case of the homogenous phantom. For the inhomogeneous phantom the necessary power outputs would be around 196, 265 and 500W, respectively. The maximum electrode power of 150W is about 5 times smaller than the typically used power range for multi-antenna systems. Consequently, using a similar electrode with a higher maximum power, the SAR level would rise appropriately. Note that more contemporary, commercially available electrodes can apply a power of >200W.

In deeper regions, we measured a TR and SAR below the aforementioned values, but it does not necessarily prove that a therapeutic effect can be excluded in such deep-seated regions. It has been described preclinically [32] and it has been confirmed by our group in cell experiments that non-thermal anticancer effects of RF-EMF based CHT exist, especially when amplitude modulation is applied [33–35]. These non-thermal anticancer effects may, in addition to the described depth-dependent TR due to CHT, explain the positive outcome in several randomized controlled trials [9–16]. Further research and clinical trials are required to study the anticancer effects of CHT for instance in body regions, where a TR is hard to be realized or even currently unfeasible treatment sited such as the liver and the brain. We have launched pilot studies to investigate this issue, which will also involve field simulations of patient models (Clinicaltrials.gov identifiers NCT06140875 and NCT05991102).

The synthetic fat layer impairs the heating in the tissue underneath, up until a depth of 8.5cm inside the phantom in its central plot in the central vertical plane (from 8.5cm onwards the absolute local TR is similar, deviations are ≤0.1°C). At the measurement point in 1cm depth inside both phantoms in their respective central plot in the central vertical plane., the TR is 36% lower for the inhomogeneous phantom when compared to the homogeneous phantom. At depths of 1.6, 2.3, 2.9, 3.5 and 4.1cm the TR is 28%, 25%, 37%, 35% and 37% lower, respectively, for the inhomogeneous phantom.

From the presented matrices (Figure 8a, b and 9a–d) it can be concluded, that in difference to Beck et al. [21], no hotspots are observed at the edge of the electrode or more precisely near the edge of electrode's water bolus that was contacting the phantom's top surface. Note, however, that a different capacitive system with a different electrode geometry was used in that study.

In addition, we were able to establish field simulations, and our SAR simulations show encouraging results, at least up to a depth of 11cm, with a difference of on average 25% for the homogeneous and 43% for the inhomogeneous phantom in their central vertical plots. This may enable our routine toward a simulation environment in Sim4Life feasible for further in silico studies with patient models.

Considering the whole central vertical plane up to a depth of 11cm and an evaluated radius of 10.5cm there is a difference of on average 35% for the homogeneous and 58% for the inhomogeneous phantom.

Figure 9a) calculated SAR homogeneous phantom

depth	horizontal position (cm)													
[cm]	-19.5	-16.5	-13.5	-10.5	-7.5	-4.5	-1.5	1.5	4.5	7.5	10.5	13.5	16.5	19.5
1	1.74	4.07	7.55	11.62	33.69	44.72	43.56	34.27	37.17	30.20	7.55	5.23	3.48	2.32
2.3	0.58	1.16	2.90	7.55	14.52	22.65	23.81	17.43	14.52	10.46	4.07	1.16	0.58	0.58
3.5	0.00	0.58	1.74	4.07	6.97	11.04	12.78	11.62	8.71	5.23	1.16	1.16	0.00	0.00
6	0.58	0.58	1.74	2.90	4.65	6.39	6.39	6.97	5.81	2.90	0.00	0.00	0.58	0.00
8.5	0.00	0.58	1.16	3.49	3.49	4.65	5.23	4.65	4.07	1.16	0.00	0.00	0.00	2.32
11	0.00	0.58	1.16	2.90	2.32	4.07	3.49	4.07	2.90	1.74	0.00	0.58	0.00	0.00
13.5	0.00	0.58	2.32	3.49	2.32	2.90	4.07	3.48	2.32	2.32	0.58	0.00	0.58	0.00
16	1.16	1.74	2.90	3.49	2.32	3.49	3.49	2.90	2.32	2.32	0.58	0.00	0.00	0.00
18.5	2.32	2.90	1.74	2.32	1.74	1.74	1.74	2.32	1.74	1.74	1.16	1.74	1.16	0.58
21	2.32	2.32	1.74	2.90	1.74	1.74	1.16	1.74	1.74	0.00	0.58	1.16	0.58	3.49

Figure 9b) calculated SAR inhomogeneous phantom

depth	horizontal position (cm)													
[cm]	-19.5	-16.5	-13.5	-10.5	-7.5	-4.5	-1.5	1.5	4.5	7.5	10.5	13.5	16.5	19.5
1														
2.25	3.49	4.07	4.65	6.97	15.10	20.33	16.84	18.59	16.84	10.46	6.39	4.65	4.07	3.49
3.5	2.90	3.48	3.48	4.65	8.13	9.87	8.13	9.87	8.13	4.65	3.48	3.48	3.48	2.32
6	2.90	2.90	3.48	3.48	3.48	3.48	3.48	3.49	3.49	3.49	3.49	4.07	3.49	2.32
8.5	2.90	2.32	3.48	3.48	2.90	3.48	3.48	2.32	3.49	2.90	3.49	3.49	3.49	2.32
11	1.74	2.90	3.48	2.90	2.90	3.48	2.90	3.49	4.07	3.49	4.07	3.49	3.49	2.32
13.5	2.32	2.32	3.48	2.90	2.90	2.90	2.90	2.90	3.48	3.48	4.07	3.49	3.49	2.32
16	2.90	2.90	3.49	2.90	2.90	2.90	2.90	2.90	3.48	2.32	3.49	3.49	3.49	2.32
18.5	2.90	2.90	3.48	2.90	2.90	2.90	2.32	2.32	2.90	2.90	3.48	2.32	3.49	2.90
21														

Figure 9c) simulated SAR homogeneous phantom														
depth	horizontal position [cm]													
[cm]	-19.5	-16.5	-13.5	-10.5	-7.5	-4.5	-1.5	1.5	4.5	7.5	10.5	13.5	16.5	19.5
1	0.04	0.38	1.44	6.18	34.98	45.34	44.89	45.04	45.72	30.56	5.54	1.40	0.38	0.08
2.3	0.08	0.45	1.38	5.02	17.69	27.96	30.40	30.38	27.60	16.16	4.61	1.33	0.40	0.11
3.5	0.14	0.44	1.29	3.98	10.97	17.95	20.73	20.65	17.55	10.24	3.74	1.25	0.50	0.15
6	0.24	0.48	1.10	2.49	5.06	7.84	9.43	9.38	7.66	4.87	2.43	1.09	0.49	0.26
8.5	0.34	0.54	0.96	1.74	2.92	4.14	4.89	4.87	4.08	2.87	1.73	0.98	0.56	0.38
11	0.45	0.59	0.88	1.34	1.96	2.55	2.91	2.90	2.53	1.95	1.36	0.91	0.62	0.48
13.5	0.49	0.62	0.83	1.12	1.46	1.77	1.94	1.94	1.76	1.47	1.15	0.88	0.68	0.54
16	0.45	0.64	0.81	1.01	1.21	1.37	1.46	1.46	1.36	1.21	1.04	0.89	0.76	0.57
18.5	0.74	0.69	0.83	0.95	1.06	1.14	1.18	1.17	1.12	1.05	0.96	0.91	0.94	0.78
21	1.48	0.76	0.90	0.94	0.97	0.99	1.00	0.99	0.97	0.94	0.90	0.88	1.08	0.00

Figure 9d) simulated SAR inhomogeneous phantom														
depth	horizontal position [cm]													
[cm]	-19.5	-16.5	-13.5	-10.5	-7.5	-4.5	-1.5	1.5	4.5	7.5	10.5	13.5	16.5	19.5
0.5	0.00	0.00	0.02	0.27	82.79	130.97	130.72	130.76	131.01	48.35	0.18	0.01	0.00	0.00
1														
2.3	0.06	0.32	1.16	4.61	16.90	22.96	23.39	23.41	22.85	15.38	4.08	1.08	0.30	0.07
3.5	0.09	0.33	1.07	3.56	14.99	14.99	16.42	16.37	14.68	9.21	3.23	1.00	0.31	0.09
6	0.16	0.36	0.89	2.14	4.42	6.67	7.82	7.76	6.47	4.16	2.00	0.83	0.34	0.15
8.5	0.25	0.41	0.76	1.42	2.39	3.36	3.93	3.89	3.27	2.28	1.34	0.71	0.38	0.23
11	0.35	0.46	0.69	1.05	1.52	1.97	2.23	2.21	1.92	1.46	0.99	0.63	0.41	0.30
13.5	0.40	0.49	0.65	0.86	1.10	1.32	1.45	1.44	1.30	1.06	0.81	0.59	0.43	0.33
16	0.40	0.53	0.62	0.74	0.87	0.98	1.03	1.03	0.96	0.85	0.71	0.58	0.46	0.34
18.5	0.79	0.59	0.61	0.67	0.72	0.76	0.78	0.78	0.75	0.71	0.65	0.58	0.52	0.40
21														

Figure 9. (a–d) Comparison in vertical planes between absolute SAR derived via Equation (2) from Figure 8a and b (a and b, respectively) and the corresponding simulated absolute SAR, for a total power of 75W (c and d, for the homogeneous, and the inhomogeneous phantoms, respectively). Note that for the inhomogeneous phantom (b and d) the depth values of 1 cm and 21 cm exactly indicate the positions of the interfaces between agar and fat. Therefore, no SAR comparison is performed for these depth values (for details of validity of Equation (2), see Section 2.8.3). For simulated SAR, additionally, the SAR directly inside the fat layer (depth 0.5 cm) is reported (d).

The heating abilities of the EHY-2030 system favorably compare with those of another CHT system previously investigated by our group, Celsius42 [21]. In fact, for the homogenous phantom, when considering the used power, electrode size and distance between the electrodes, in a normalization to the equal power density approach, the EHY-2030 system shows almost a 2.7-fold higher SAR in a depth of 1cm [21]. A difference in favor of the EHY-2030 can also be observed, when comparing the SAR in the inhomogeneous phantoms in 1cm depth scaled to an equal surface power density. Here, the SAR for the EHY-2030 is almost 60% higher than for the Celsius42.

Those points can be contextualized with the earlier mentioned clinical trial utilizing the EHY-2030. There, the authors report that a temperature of 42.5°C was set as the target temperature during the treatments, and the energy output from the first electrode was compared to the energy received from the 2nd electrode, and, using algorithms, the device calculated the intratumoral temperature.

Contrary, in an older study performed on a smaller amount of 11 patients with deep-seated pelvic tumors with a different CHT device operating at 13.56MHz, the temperature was measured with thermal probes inserted into the tumor and normal tissue [8]. Their subcutaneous fat layers were 1.5cm (anteriorly) and 2.1cm (posteriorly thick on average. There, for 60% of the patients, the intratumoral temperature was lower than 40°C and thus lower than what would be considered as ‘classic hyperthermia’. Fitting well to our simulations for the inhomogeneous phantom, the authors

of this study report that in 53% of the treatments the maximum temperature was measured in the subcutaneous fat. This further highlights the crucial role of surface cooling, which was also shown to reduce the temperature of the subcutaneous fat tissue [8].

Moreover, it has to be noted that the BMI was no predictor of LDC in that South African clinical trial. This also adds to the line of thought that sole heating of the tumor might not be the only physical parameter responsible for the positive results [12].

When considering a physical variable to measure the aforementioned effects on a cellular level, the current density may be a suitable parameter. The current density is a vector parameter, whereas the SAR is a scalar one. However, as the current density is proportional to the E-field rather than to the square E-field, its relative behavior can be approximately calculated based on the square root of the SAR values of our measurements. We propose further investigation, for instance to study a potential correlation between current density and cancer outcome.

Finally, it is worth noting that, even if we designed our pilot study using similar geometry and heating time to those proposed by the ESHO guidelines, the main aim of this study was not to judge on the thermal effectivity of this system via a strict fulfillment of the procedures and temperature limits defined by the ESHO guidelines. This study has to be understood as a pilot study to check the feasibility of the phantom production and use of the splitting technique, as well as to perform comparisons with numerical results. Furthermore, as only one electrode was used in this study, the final characterization of the system cannot be claimed. Moreover, we do not claim to decide if the system is 'thermally efficient' or not. Note that the system's driving power limitation with respect to both electrodes is rather conservative and, as it was already stated above, there are, in principle, no technical limitations for using higher powers than 150W for the D200 electrode, if necessary (note that the exchangeable bigger D300 electrode of the system is capable of using 250W). In general, hyperthermia is a multifaceted treatment so full clinical usefulness of a complex medical device is not only dependent on a single number like 'ability of heating of 6 degrees Celsius in 6min'. Moreover, measurements were taken in phantoms instead of patients in which, for instance, blood perfusion adds to the cooling and cooling inhomogeneity. On the other side, a synthetic 'fat' layer was used for the inhomogeneous phantom in our paper that is not equal to the real fat tissue, and thus higher SAR values may be expected in real fat. Again, an open question is if these higher SAR values would 'automatically' lead to higher temperature, when blood perfusion is present. Further studies should be performed to fully characterize the heating abilities of CHT devices, using both phantom and real patient set-ups.

5. Conclusion

Computer simulations and experimental data were compared for the CHT system EHY-2030 using the D200 electrode, applying a thermal imaging technique for different vertically splittable phantoms. In this pilot study the system power of 75W was chosen, which is half of the maximum power of 150W and lies in the range of usual values for this electrode applied in patient treatments in our clinic. For 75W, a heating of 3.6°C in 6min in a depth of 1cm in the central plot in the central vertical plane in an agar-based, muscle tissueequivalent phantom was achieved. The addition of a 1cm thick, synthetic, low dielectric fat layer reduced the TR in the central plot in the central vertical plane up until a depth of 8.5cm by on average around 38% (from 8.5cm onwards the absolute local

TR is similar, deviations are ≤0.1°C). Measured results have been compared with simulations. For a full characterization of this system, further studies involving the large electrode D300 and larger phantoms suited for this electrode are needed. Moreover, further studies should be performed to fully characterize the heating abilities of CHT devices, using both phantom and real patient set-ups.

Acknowledgments
We thank Oncotherm Kft, Budapest, Hungary for their support of our research and providing the clinical device. We thank Jan-Erik Ode and Alexander Schill from Centrum Wissenschaftliche Werkstätten (CWW), Charité Universitätsmedizin Berlin for their technical support. Andrea Stroux supported biometric analyses.

Disclosure statement
PG received research funding from Oncotherm Kft, Budapest, Hungary and Dr. Sennewald Medizintechnik GmbH, München, Germany. PG received consultancy fees from Dr. Sennewald Medizintechnik GmbH, München, Germany and from Sensius, Rotterdam, The Netherlands. JN received consultancy fees from Dr. Sennewald Medizintechnik GmbH, München, Germany and from Sensius, Rotterdam, The Netherlands. There are no further conflicts of interest to disclose.

Funding
PDV is supported by the H2020 Marie Sklodowska-Curie program – HYPERBOOST (project number: 955625).

ORCID
Jacek Nadobny http://orcid.org/0000-0002-0520-7719
Pirus Ghadjar http://orcid.org/0000-0002-2747-165X

Data availability statement
The data that support the findings of this study are available from the corresponding author, [PG], upon reasonable request.

References

[1] van der Zee J, González González D, van Rhoon GC, et al. Comparison of radiotherapy alone with radiotherapy plus hyperthermia in locally advanced pelvic tumours: a prospective, randomised, multicentre trial. Dutch Deep Hyperthermia Group. Lancet. 2000;355(9210):1119– 1125. doi:10.1016/S0140-6736(00)02059-6.

[2] Overgaard J, Gonzalez Gonzalez D, Hulshof MC, et al. Randomised trial of hyperthermia as adjuvant to radiotherapy for recurrent or metastatic malignant melanoma. European Society for Hyperthermic Oncology. Lancet. 1995;345(8949):540–543. doi:10.1016/s0140-6736 (95)90463-8.

[3] Jones EL, Oleson JR, Prosnitz LR, et al. Randomized trial of hyperthermia and radiation for superficial tumors. J Clin Oncol. 2005; 23(13):3079–3085. doi:10.1200/JCO.2005.05.520.

[4] Issels RD, Lindner LH, Verweij J, et al. Effect of neoadjuvant chemotherapy plus regional hyperthermia on long-term outcomes among patients with localized high-risk soft tissue sarcoma. JAMA Oncol. 2018;4(4):483–492. doi:10.1001/jamaoncol.2017.4996.

[5] Wust P. Thermotherapy in Oncology. Bremen, Germany: UNI-MED Verlag AG; 2016.

[6] Issels R, Kampmann E, Kanaar R, et al. Hallmarks of hyperthermia in driving the future of clinical hyperthermia as targeted therapy: translation into clinical application. Int J Hyperthermia. 2016;32(1): 89–95. doi:10.3109/02656736.2015.1119317.

[7] Wust P, Hildebrandt B, Sreenivasa G, et al. Hyperthermia in combined treatment of cancer. Lancet Oncol. 2002;3(8):487–497. doi:10. 1016/S1470-2045(02)00818-5.

[8] van Rhoon GC, van der Zee J, Broekmeyer-Reurink MP, et al. Radiofrequency capacitive heating of deep-seated tumours using pre-cooling of the subcutaneous tissues: results on thermometry in Dutch patients. Int J Hyperthermia. 1992;8(6):843–854. doi:10. 3109/02656739209005031.

[9] Chi M-S, Yang K-L, Chang Y-C, et al. Comparing the effectiveness of combined external beam radiation and hyperthermia versus external beam radiation alone in treating patients with painful bony metastases: A phase 3 prospective, randomized, controlled trial. Int J Radiat Oncol Biol Phys. 2018;100(1):78–87. doi:10.1016/j.ijrobp.2017.09.030.

[10] Huilgol NG, Gupta S, Sridhar CR. Hyperthermia with radiation in the treatment of locally advanced head and neck cancer: a report of randomized trial. J Can Res Ther. 2010;6(4):492–496. doi:10. 4103/0973-1482.77101.

[11] Datta NR, Bose AK, Kapoor HK, et al. Head and neck cancers: results of thermoradiotherapy versus radiotherapy. Int J Hyperthermia. 1990;6(3):479–486. doi:10.3109/02656739009140944.

[12] Minnaar CA, Maposa I, Kotzen JA, et al. Effects of modulated electro-hyperthermia (mEHT) on two and three year survival of locally advanced cervical cancer patients. Cancers (Basel). 2022;14(3): 656. doi:10.3390/cancers14030656.

[13] Harima Y, Nagata K, Harima K, et al. A randomized clinical trial of radiation therapy versus thermoradiotherapy in stage IIIB cervical carcinoma. Int J Hyperthermia. 2009;25(5):338–343. doi:10.1080/02656730903092018.

[14] Harima Y, Ohguri T, Imada H, et al. A multicentre randomised clinical trial of chemoradiotherapy plus hyperthermia versus chemoradiotherapy alone in patients with locally advanced cervical cancer. Int J Hyperthermia. 2016;32(7):801–808. doi:10.1080/02656736.2016.1213430.

[15] Nishimura Y, Hiraoka M, Akuta K, et al. Hyperthermia combined with radiation therapy for primarily unresectable and recurrent colorectal cancer. Int J Radiat Oncol Biol Phys. 1992;23(4):759–768. doi:10.1016/0360-3016(92)90649-3.

[16] Minnaar CA, Kotzen JA, Ayeni OA, et al. The effect of modulated electro-hyperthermia on local disease control in HIV-positive and -negative cervical cancer women in South Africa: early results from a phase III randomised controlled trial. PLoS One. 2019;14(6): e0217894. doi:10.1371/journal.pone.0217894.

[17] Wang Y, Hong W, Che S, et al. Outcomes for hyperthermia combined with concurrent radiochemotherapy for patients with cervical cancer. Int J Radiat Oncol Biol Phys. 2020;107(3):499–511. doi:10.1016/j.ijrobp.2020.03.006.

[18] Vasanthan A, Mitsumori M, Park JH, et al. Regional hyperthermia combined with radiotherapy for uterine cervical cancers: a multi-institutional prospective randomized trial of the international atomic energy agency. Int J Radiat Oncol Biol Phys. 2005;61(1):145– 153. doi:10.1016/j.ijrobp.2004.04.057.

[19] Hiraoka M, Jo S, Akuta K, et al. Radiofrequency capacitive hyperthermia for deep-seated tumors. I. Studies on thermometry. Cancer. 1987;60(1):121–127. doi:10.1002/1097-0142(19870701)60:13.0.CO;2-I.

[20] Kato H, Hiraoka M, Nakajima T, et al. Deep-heating characteristics of an RF capacitive heating device. Int J Hyperthermia. 1985;1(1):15– 28. doi:10.3109/02656738509029271.

[21] Beck M, Wust P, Oberacker E, et al. Experimental and computational evaluation of capacitive hyperthermia. Int J Hyperthermia. 2022;39(1):504–516. doi:10.1080/02656736.2022.2048093.

[22] Nakahara S, Ohguri T, Kakinouchi S, et al. Intensity-modulated radiotherapy with regional hyperthermia for high-risk localized prostate carcinoma. Cancers (Basel). 2022;14(2):400. doi:10.3390/cancers14020400.

[23] Dobšíček Trefná H, Crezee J, Schmidt M, et al. Quality assurance guidelines for superficial hyperthermia clinical trials: II. Technical requirements for heating devices. Strahlenther Onkol. 2017;193(5): 351–366. doi:10.1007/s00066-017-1106-0.

[24] Kok HP, Crezee J. Validation and practical use of Plan2Heat hyperthermia treatment planning for capacitive heating. Int J Hyperthermia. 2022;39(1):952–966. doi:10.1080/02656736.2022.2093996.

[25] Kato H, Hiraoka M, Ishida T. An agar phantom for hyperthermia. Med Phys. 1986;13(3):396–398. doi:10.1118/1.595882.

[26] Mattia De Lazzari AS, Farina L, Silva NP, et al. Ethylcellulose-stabilized fat-tissue phantom for quality assurance in clinical hyperthermia. Int J Hyperthermia. 2023;40(1):2207797. doi:10.1080/02656736.2023. 2207797.

[27] Pennes HH. Analysis of tissue and arterial blood temperatures in the resting human forearm. 1948. J Appl Physiol (1985). 1998;85(1): 5–34. doi:10.1152/jappl.1998.85.1.5.

[28] Nadobny J, Szimtenings M, Diehl D, et al. Evaluation of MR-induced hot spots for different temporal SAR modes using a time-dependent finite difference method with explicit temperature gradient treatment. IEEE Trans Biomed Eng. 2007;54(10):1837–1850. doi:10.1109/TBME.2007.893499.

[29] Bianchi L, Cavarzan F, Ciampitti L, et al. Thermophysical and mechanical properties of biological tissues as a function of temperature: a systematic literature review. Int J Hyperthermia. 2022;39(1): 297–340. doi:10.1080/02656736.2022.2028908.

[30] Kevin Cole JB, Haji-Sheikh A, Litkouhi B. Heat conduction using green's functions. 2nd ed. Boca Raton (FL): CRC Press; 2011.

[31] Wust P, Stahl H, Löffel J, et al. Clinical, physiological and anatomical determinants for radiofrequency hyperthermia. Int J Hyperthermia. 1995;11(2):151–167. doi:10.3109/02656739509022453.

[32] Krenacs T, Meggyeshazi N, Forika G, et al. Modulated electrohyperthermia-induced tumor damage mechanisms revealed in cancer models. Int J Mol Sci. 2020;21(17):6270. doi:10.3390/ijms21176270.

[33] Wust P, Veltsista PD, Oberacker E, et al. Radiofrequency electromagnetic fields cause non-temperature-induced physical and biological effects in cancer cells. Cancers (Basel). 2022;14(21):5349. doi: 10.3390/cancers14215349.

[34] Wust P, Stein U, Ghadjar P. Non-thermal membrane effects of electromagnetic fields and therapeutic applications in oncology. Int J Hyperthermia. 2021;38(1):715–731. doi:10.1080/02656736.2021.1914354.

[35] Wust P, Kortüm B, Strauss U, et al. Non-thermal effects of radiofrequency electromagnetic fields. Sci Rep. 2020;10(1):13488. doi:10. 1038/s41598-020-69561-3.